

Accepted by ApJ

Arcsecond-Resolution Submillimeter HCN Imaging of the Binary Protostar IRAS 16293-2422

Shigehisa Takakuwa^{1,2}, Nagayoshi Ohashi³, Tyler L. Bourke⁴, Naomi Hirano³, Paul T. P. Ho^{3,4}, Jes K. Jørgensen⁴, Yi-Jehng Kuan^{3,5}, David J. Wilner⁴, Sherry C. C. Yeh³

ABSTRACT

With the Submillimeter Array (SMA) we have made high angular-resolution ($\sim 1'' = 160$ AU) observations of the protobinary system IRAS 16293-2422 in the $J = 4 - 3$ lines of HCN and HC^{15}N , and in the continuum at 354.5 GHz. The HCN (4-3) line was also observed using the JCMT to supply missing short spacing information. Submillimeter continuum emission is detected from the individual binary components of Source A in the South-East and Source B in the North-West with a separation of $\sim 5''$. The optically-thin HC^{15}N (4-3) emission taken with the SMA has revealed a compact (~ 500 AU) flattened structure (P.A. = -16°) associated with Source A. This compact structure shows a velocity gradient along the projected minor axis, which can be interpreted as an infalling gas motion. Our HCN image including the short-spacing information shows an extended (~ 3000 AU) circumbinary envelope as well as the compact structure associated with Source A, although the P.A. of the compact structure ($= -45^\circ$) seen in the HCN emission is slightly different from that of the HC^{15}N emission. A toy model consisting of a flattened structure with radial infall towards a $1 M_\odot$ central star reproduces the HCN/ HC^{15}N position-velocity diagram along the minor axis of the HC^{15}N emission. In the extended envelope there is also a North-East

¹Harvard-Smithsonian Center for Astrophysics, Submillimeter Array Project, 645 North A'ohoku, Hilo, HI 96720, U.S.A.

²Present Address: National Astronomical Observatory of Japan, ALMA Project Office, Osawa 2-21-1, Mitaka, Tokyo, 181-8588, Japan, e-mail: s.takakuwa@nao.ac.jp

³Academia Sinica Institute of Astronomy and Astrophysics, P.O. Box 23-141, Taipei 106, Taiwan

⁴Harvard-Smithsonian Center for Astrophysics, 60 Garden Street, Cambridge, MA 02138, U.S.A.

⁵Department of Earth Sciences, National Taiwan Normal University, 88 Sec.4, Ting Chou Rd., Taipei 116, Taiwan

(Blue) to South-West (Red) velocity gradient across the binary alignment, which is likely to reflect gas motion in the swept-up dense gas associated with the molecular outflow from Source A. At Source B, there is only a weak compact structure with much narrower line widths ($\sim 2 \text{ km s}^{-1}$) seen in the optically-thin HC^{15}N emission than that at Source A ($> 10 \text{ km s}^{-1}$), and there is no clearly defined bipolar molecular outflow associated with Source B. These results imply the different evolutionary stages between Source A and B in the common circumbinary envelope. Our study demonstrates the importance of adding short spacing data to interferometer data in order to probe the detailed structure and kinematics from extended ($> 3000 \text{ AU}$) envelopes to inner compact ($< 500 \text{ AU}$) structures around low-mass protostars.

Subject headings: ISM: individual (IRAS 16293-2422) — ISM: molecules — stars: disk — stars: formation

1. Introduction

Millimeter molecular-line observations have found 2000–10000 AU scale molecular envelopes around low-mass protostars (Benson & Myers 1989; Zhou et al. 1989; Blake et al. 1994; Zhou et al. 1994; Blake et al. 1995; Hogerheijde et al. 1997; Hogerheijde et al. 1999; Takakuwa et al. 2000; Takakuwa et al. 2003b), and detailed interferometric studies in millimeter lines have revealed rotating and infalling gas motion in these envelopes (Ohashi et al. 1996; Ohashi et al. 1997a; Ohashi et al. 1997b; Momose et al. 1998). The dense and warm innermost ($\leq 500 \text{ AU}$) region of these low-mass protostellar envelopes is a likely site of formation of protoplanetary disks around protostars (Terebey et al. 1993; Beckwith & Sargent 1996). However, there is not a great deal of information published about the connection between large-scale protostellar envelopes and small-scale disks around the central protostars. With the advent of interferometers in the millimeter and centimeter wavelengths and the use of multiple spectral lines, progress is being made toward separating the warm and dense regions from the overlying lower-density and colder gas along the line of sight (Mundy et al. 1990; Momose et al. 1998; Fuller & Wootten 2000; Hogerheijde 2001; Takahashi et al. 2006). Recent arcsecond or subarcsecond-resolution millimeter interferometric observations have enabled us to investigate the innermost regions of protostellar envelopes (Looney et al. 2000; Beltrán et al. 2004; Bottinelli et al. 2004). Detailed submillimeter line observations are also useful for these studies, since submillimeter molecular lines such as HCN (4–3) trace higher densities ($> 10^8 \text{ cm}^{-3}$) and temperatures ($> 40 \text{ K}$). Earlier studies of low-mass protostel-

lar envelopes with the Submillimeter Array (SMA)¹ have demonstrated that submillimeter interferometric observations are uniquely suited to probe the innermost part of low-mass protostellar envelopes (Kuan et al. 2004; Takakuwa et al. 2004; Chandler et al. 2005; Bourke et al. 2005; Jørgensen et al. 2005). We note that in order to study the connection between the large-scale envelopes and inner disks, observations that sample adequately the emission from large to small scales with high enough resolution are needed (Gueth et al. 1996; Welch et al. 2000; Takakuwa et al. 2004; Takahashi et al. 2006).

IRAS 16293-2422 (hereafter I16293) is a Class 0 protobinary system with a projected separation of ~ 800 AU (Source A and Source B) (Wootten 1989; Mundy et al. 1992; Looney et al. 2000) in the Ophiuchus Molecular Cloud, surrounded by an ~ 8000 AU-scale circumbinary envelope (Schöier et al. 2002; Stark et al. 2004). Previous SMA observations reported by Chandler et al. (2005) further demonstrate that one of the binary components, Source A, may be composed of at least three components within a $1''$ region. It has been reported that there is rotating and infalling gas motion in the circumbinary envelope of I16293 (Walker et al. 1986; Menten et al. 1987; Zhou 1995; Narayanan et al. 1998; Ceccarelli et al. 2000a; Schöier et al. 2002). Large-scale quadrupolar molecular outflows have been observed in I16293 (Walker et al. 1988; Mizuno et al. 1990; Castets et al. 2001; Hirano et al. 2001; Garay et al. 2002; Stark et al. 2004). Previous interferometric (Bottinelli et al. 2004; Kuan et al. 2004; Schöier et al. 2004; Chandler et al. 2005; Huang et al. 2005) and single-dish molecular-line observations (Blake et al. 1994; van Dishoeck et al. 1995; Ceccarelli et al. 2000b; Schöier et al. 2002; Cazaux et al. 2003; Schöier et al. 2004) have revealed a number of complex organic molecules and hot-core chemistry in I16293. Previous published SMA observations (Chandler et al. 2005) have studied in detail the structure and kinematics in the circumbinary envelope and circumstellar disks for each binary companion, the driving sources of the outflows, and the evolutionary status of each member of the binary.

In this paper, we describe results of HCN (4–3), HC¹⁵N (4–3), and 354.5 GHz continuum observations of I16293 made with the SMA and James Clerk Maxwell Telescope (JCMT). This paper focuses on sampling, as completely as we can, the structure and kinematics from the large-scale (~ 3000 AU) circumbinary envelope traced by JCMT to the smaller-scale (≤ 500 AU) structures traced with the SMA. For comparison with previous studies we assume a distance of 160 pc to the Ophiuchus cloud (Whittet 1974), but we note that more recent studies locate the cloud at a nearer distance of 120–140 pc (de Geus et al. 1989; Knude & Høg 1998).

¹The Submillimeter Array (SMA) is a joint project between the Smithsonian Astrophysical Observatory and the Academia Sinica Institute of Astronomy and Astrophysics, and is funded by the Smithsonian Institution and the Academia Sinica.

2. Observations

2.1. Submillimeter Array Observations

With the Submillimeter Array (SMA) we made HCN ($J = 4-3$; 354.5055 GHz), HC ^{15}N ($J = 4-3$; 344.200122 GHz), and 354.5 GHz continuum observations of I16293 on 2003 March 14, July 12, and 2004 June 19. Details of the SMA are described by Ho, Moran, & Lo (2004). The SMA is a double-sideband instrument, and the HCN and HC ^{15}N lines were observed simultaneously in different sidebands. We assigned a spectral window of the SMA correlator (“chunk”) with a spectral resolution of 0.17 km s^{-1} to the HCN line, and a chunk with a resolution of 0.71 km s^{-1} to the HC ^{15}N line². Table 1 summarizes the observational parameters. The observations were made in three different array configurations to provide well-sampled (u, v) coverage. The range of the baseline length projected on the sky was from $\sim 10 \text{ k}\lambda$ to $\sim 223 \text{ k}\lambda$, and our observations were insensitive to structures more extended than $\sim 16''.5$ ($\sim 2600 \text{ AU}$) at the 10% level (Wilner & Welch 1994). We confirmed that the visibility amplitudes of the continuum emission from I16293 from the three observing periods were consistent within the noise level. The overall flux uncertainty was estimated to be $\sim 30\%$. Part of the 2003 data set has already been published by Kuan et al. (2004) and Huang et al. (2005), which is of lower angular resolution than the full data set presented here.

The raw visibility data were calibrated and flagged with MIR, which is an IDL-based reduction package adopted for the SMA from the MMA software package developed originally for the Owens Valley Radio Observatory (Scoville et al. 1993). The calibrated visibility data were Fourier-transformed and CLEANed with MIRIAD to produce images (Sault et al. 1995). The spatial resolution is $1''.1 \times 0''.6$ (P.A. = 39°), $1''.3 \times 1''.2$ (P.A. = 30°), and $1''.6 \times 1''.3$ (P.A. = 14°), in the 354.5 GHz continuum, HCN, and HC ^{15}N images, respectively. The spatial resolution of the HCN image is set to be the same as that of the combined SMA + JCMT image (see next section), in order to directly compare the SMA and combined images and to see the effect of missing short-spacings.

2.2. James Clerk Maxwell Telescope Observations

Submillimeter single-dish mapping observations of I16293 in the HCN (4–3) line were made with the James Clerk Maxwell Telescope (JCMT) on 2004 March 7 and April 7. The JCMT beam size at 354 GHz band was $\sim 15''$ and the typical system temperature was 600

²Due to the instrumental constraint of the SMA correlator, it is not possible to assign the high-resolution chunk to both the HCN and HC ^{15}N lines.

K. We observed a 7×7 map centered on the field center of the SMA observations at a grid spacing of $7''.5$, providing a Nyquist-sampled map in the $45'' \times 45''$ region. Each position in the map was observed for 1 minute and the map was repeated 6 times. The central map position was observed at the start, middle and end of each map as a check on the relative flux calibration. The observations were made in dual-polarization mode, and the 2 polarizations averaged, resulting in an rms noise level per 0.13 km s^{-1} channel of $\sim 0.13 \text{ K}$ in T_A^* . Pointing and focusing were checked before each set of maps. The conversion factor from T_A^* (K) to S (Jy beam^{-1}) was derived to be 36.7 as;

$$S = \frac{2k_B \Omega_{beam}}{\lambda^2} \frac{T_A^*}{\eta_{mb}}, \quad (1)$$

where k_B is the Boltzmann constant, Ω_{beam} is the solid angle of the JCMT beam ($= 15''$), λ is the wavelength, and η_{mb} is the main beam efficiency of the JCMT ($= 0.63$). The mapped region covers well the field of view of the SMA observations ($\sim 35''$), which enables us to compare the JCMT flux to the SMA flux. The SMA observations recovered $\sim 35\%$ (Source A) and 31% (Source B) of the total HCN(4-3) flux observed with the JCMT toward the binary system (The JCMT observations do not resolve the $5''$ binary). We combined the JCMT data with the SMA data, and in the subsequent sections we will mainly discuss the combined images. The details of the combining process are described in Appendix. The resultant synthesized beam size and the rms noise level in the combined images is $1''.3 \times 1''.2$ (P.A. = 30°) and $\sim 0.90 \text{ Jy beam}^{-1} \text{ channel}^{-1}$, respectively, where the velocity resolution is the same as that of the SMA data.

3. Results

3.1. Submillimeter Continuum Emission

In Figure 1 we show our 354.5 GHz continuum image of I16293. Previous SMA images of the continuum emission in I16293 at somewhat lower angular resolutions have been presented in Kuan et al. (2004) and Chandler et al. (2005; although they subsequently improved their resolution through “super-resolution” imaging techniques, discussed below). Submillimeter continuum emission from the individual binary protostars, called Source A (south-east) and B (north-west) (Mundy et al. 1992), are evident. The total continuum fluxes at 354.5 GHz are 3840 and 4050 mJy at Source A and B, respectively, which are slightly higher than the continuum fluxes at 305 GHz (3460 and 3150 mJy at Source A and B; Chandler et al. 2005). Chandler et al. (2005) reported that the spectral indexes ($\equiv \alpha$)

in the millimeter and submillimeter regime are 2.91 and 2.51 at Source A and B, respectively. We re-estimated the spectral indexes including our new submillimeter measurements, and the values are 2.87 and 2.68 at Source A and Source B, respectively. These values are consistent with the values by Chandler et al. (2005) within the uncertainties ($\sim \pm 0.1$). The submillimeter continuum emission at Source A shows evidence of extension along the North-East to South-West direction, while that at Source B is more compact. In Table 2, we summarize the properties of the submillimeter continuum emission from both protostars after the deconvolution of the synthesized beam. Using “super-resolution” imaging by only using data with uv distance greater than $55 k\lambda$, the extension at Source A is resolved into two components with the SMA (Aa and Ab; Chandler et al. 2005), possibly a close binary system. The peak positions of the 354.5 GHz continuum emission are slightly ($\sim 0''.4$) offset from the 115 GHz (Looney et al. 2000) and 300 GHz (Chandler et al. 2005) continuum positions, presumably due to the limited calibration accuracy of our higher-frequency observations. Detailed multi-wavelength (230-690 GHz) analysis of the submillimeter continuum emission will be presented in a forthcoming paper.

3.2. Spatial and Velocity Distribution of the HCN and HC^{15}N Emission

In Figure 2, we compare the HCN (4–3) line profiles from SMA and combined SMA+JCMT data at Source A and B, along with the SMA HC^{15}N (4–3) line profiles. We also show the average (Source A + Source B) SMA and SMA+JCMT spectra for comparison with the JCMT HCN spectrum. The HCN (4–3) line profiles show two emission peaks with a brighter blue-shifted peak and an absorption dip. The SMA and combined HCN spectra show a larger brightness temperature with more prominent wing-like emission as compared to those obtained with the JCMT, while the interferometric-only spectra systematically miss lower-velocity emission around $V_{LSR} = 2 - 4 \text{ km s}^{-1}$ as compared to the combined spectra, particularly at Source A. The dip in the SMA+JCMT and the SMA spectra seems to show absorptions against the continuum. The HC^{15}N spectra shown in Figure 2 include new data taken on June 19, 2004 as compared to the HC^{15}N spectra shown by Kuan et al. (2004), and the spatial resolution ($\sim 1''.6 \times 1''.3$) is higher than that of Kuan et al. (2004) ($\sim 2''.7 \times 1''.3$). At Source A, the HC^{15}N line profile shows a single peak near the dip velocity. The centroid velocity of the HC^{15}N line at Source A is estimated to be $\sim 2.9 \text{ km s}^{-1}$ from a single-component Gaussian fitting to the spectrum. At Source B, there is a weak ($\sim 4\sigma$) HC^{15}N emission near the centroid velocity. This velocity is slightly bluer than the HCN dip velocity ($\sim 4.3 \text{ km s}^{-1}$), although the coarser velocity resolution of the HC^{15}N data ($\sim 0.71 \text{ km s}^{-1}$) prevents us from making the direct comparison between the HCN and HC^{15}N velocities. Taking into account the coarse velocity resolution in the HC^{15}N

line, we adopt the symmetric velocity of the HCN Position-Velocity diagram (Figure 7) as a systemic velocity ($\sim 3.6 \text{ km s}^{-1}$). At this velocity, the HCN (SMA+JCMT)/HC¹⁵N (SMA) line intensity ratio toward Source A is ~ 4 , which implies an optical depth of ~ 0.3 for the HC¹⁵N line assuming an N¹⁴/N¹⁵ isotopic ratio of 270 (Lucas & Liszt 1998). Therefore, the HC¹⁵N line is likely to be optically thin. The redshifted self-absorption in the HCN spectra against the continuum at Source A could be a sign of the inward motion toward the continuum source (Zhou 1992; Myers et al. 1995; Narayanan et al. 1998; Di Francesco et al. 2001; Schöier et al. 2002; Stark et al. 2004), although the presence of the extended HCN absorption in the entire region (See Figure 4) implies significant contamination from extended low-temperature material. The red-shifted self-absorption from the systemic velocity can be reproduced using models of infalling cores with the Larson-Penston flow (Larson 1969; Penston 1969), as has been shown by Masunaga & Inutsuka (2000). Such a red-shifted dip was also detected in B335 (Choi et al. 1999; Evans et al. 2005), which is one of the most well-studied infalling cores.

Figure 3 shows two different HCN integrated intensity maps; one made using only the SMA data (left), and the other made using the JCMT and SMA combined data (middle). Figure 3 also shows the HC¹⁵N integrated intensity map taken with the SMA for comparison (right). The continuum emission has been subtracted before forming these maps. In the optically-thin HC¹⁵N emission there is a compact emission associated with Source A. From a 2-dimensional Gaussian fitting to the image, the FWHM size of this compact HC¹⁵N emission after the deconvolution of the synthesized beam is $450 \text{ AU} \times 250 \text{ AU}$ (P.A. = -16°). A similar compact structure is also seen in the SMA and combined SMA+JCMT HCN images with a size of $630 \text{ AU} \times 320 \text{ AU}$ (P.A. = -43°) and $740 \text{ AU} \times 440 \text{ AU}$ (P.A. = -45°), respectively, although the P.A. of the HCN component is slightly different from that of the HC¹⁵N emission. The HCN emission also shows extensions to the North-West and to the North-East of Source A in addition to this compact structure. Importantly, the combined HCN image shows that all of these features are surrounded by a halo component with a size of $\sim 3000 \text{ AU}$, demonstrating that the SMA is not sensitive to the extended structure. This halo structure is most likely a molecular envelope surrounding the I16293 protobinary system. Similar extended structures are also seen in the H₂CO (4_{1,3}–3_{1,2}) and SO (7_{7–6}) emission, although the detailed distributions are somewhat different from each other (Chandler et al. 2005).

In Figure 4, we present velocity channel maps of the SMA+JCMT HCN data. At high blueshifted velocities ($-2.8 \text{ km s}^{-1} < V_{LSR} < -1.2 \text{ km s}^{-1}$), there is a compact gas component associated with Source A. This high-velocity component corresponds to the compact structure seen in the total integrated intensity map of Figure 3. From $V_{LSR} = -0.73 \text{ km s}^{-1}$, a secondary component is seen at the south-east of Source B. From $V_{LSR} \sim 1.9 \text{ km s}^{-1}$, an

extended halo component appears until $V_{LSR} = 4.4 \text{ km s}^{-1}$, where little emission is evident due to the extended self-absorption in the HCN emission. After this velocity the redshifted halo component appears again. From $V_{LSR} \sim 6.5 \text{ km s}^{-1}$ a compact gas component toward Source A is seen, which corresponds to the redshifted counterpart of the compact structure at Source A.

In order for us to see the systematic velocity structures more clearly, we integrated these velocity channel maps into four different velocity regimes, that is, low-velocity blueshifted ($2.5 - 3.4 \text{ km s}^{-1}$) and redshifted ($5.0 - 6.5 \text{ km s}^{-1}$), and high-velocity blueshifted ($-2.6 - 0.7 \text{ km s}^{-1}$) and redshifted ($7.4 - 9.1 \text{ km s}^{-1}$) emission. In Figure 5, we compare these four HCN velocity channel maps to the CO (2–1) maps taken with the SMA (Yeh et al. 2007), integrated into the same four velocity regimes. The spatial resolution in the CO (2–1) map is $3''.3 \times 2''.0$ (P.A. = 40°). In the low-velocity regimes, the overall distributions of the HCN emission, which shows extended halo structures, are very similar to those of the CO (2–1) emission. This suggests that the extended halo structures are affected by a low-velocity outflow or turbulent gas traced by CO. The redshifted halo component appears mostly at the south-west and south-east of the binary, while the blueshifted halo component at the north-east and north-west of the binary. In the high velocity regimes, the HCN emission shows extensions as well as the compact structures associated with Source A. The comparison with the CO maps shows that the HCN extensions have distributions similar to those of CO, particularly at the high redshifted velocity. This suggests that the HCN extensions are also affected by the high-velocity outflow. On the other hand, the compact HCN emission associated with Source A seems to show different distributions from those of CO, which suggests that it has different origin. The compact HCN component is also distinct from the more extended low-velocity emission. We will discuss the origin of these different velocity components in the next section.

4. Discussion

4.1. Origin of the Different Velocity Structures

Our SMA and JCMT observations have revealed a high-velocity compact ($\sim 500 \text{ AU}$) structure associated with Source A and an extended ($\sim 3000 \text{ AU}$) low-velocity circumbinary envelope around sources A and B. In this subsection, the origin of these different velocity structures is discussed.

In Figure 6, we compare the high-velocity blueshifted and redshifted HCN and HC^{15}N emission to the CO (2–1) outflow map taken with the SMA (Yeh et al. 2007). As discussed

in Yeh et al. (2007), source A is the most likely to be driving the E-W CO outflow, while the driving source of the NW-SE outflow remains uncertain. In the optically-thin HC^{15}N emission, the high-velocity blueshifted and redshifted components exhibit a velocity gradient along the minor axis (P.A. 74°) of the compact HC^{15}N structure. The velocity gradient along the minor axis is approximately parallel to the E-W CO outflow, though the position angle of the E-W CO outflow can not be well-defined due to the wide opening angle. Although the direction of the minor axis of the compact HCN emission is slightly different from that of the compact HC^{15}N emission, the direction of the velocity gradient in the HCN emission is similar to that of the HC^{15}N emission. One possible interpretation of the observed velocity gradient in the compact flattened structure is outflowing gas, because both the CO outflow and the HCN/ HC^{15}N emission show the same trend of velocity gradient. In fact, the extended HCN emission is strongly affected by the molecular outflow, as has been discussed in the previous section. The slight difference of the position angle between the compact HCN and HC^{15}N component is also likely to be due to the contamination from the extended component. However, the optically-thin HC^{15}N emission, which should be less affected by the extended outflow component, is clearly elongated in a different direction from the outflow direction (Figure 5 and 6), suggesting that the velocity gradient is unlikely to be due to the outflow. We interpret the observed velocity gradients in the HCN and HC^{15}N emission to be an infalling gas motion in the flattened disklike structure toward Source A (Hayashi et al. 1993; Ohashi et al. 1996; Momose et al. 1998).

In the left panel of Figure 7, we show position-velocity (P-V) diagrams along the minor axis of the HC^{15}N compact emission at Source A (see Figure 6), in the HCN emission with the SMA-only (gray) and SMA+JCMT (black contour), and in the HC^{15}N emission with the SMA (red contour). In the P-V diagrams, both the HCN and HC^{15}N lines trace the higher-velocity emission located close to Source A, and this velocity structure corresponds to the compact emission at Source A. We made a number of model P-V diagrams of a geometrically thin disk with Gaussian intensity distribution to reproduce this component, one of which is shown in the right panel of Figure 7. From the estimated major and minor axis in the SMA HC^{15}N image we estimated the inclination angle of the flattened structure from the plane of the sky to be $\sim 57^\circ$ ($\equiv \cos^{-1}(\text{maj}/\text{min})$), and we adopted this inclination in the model P-V diagram. We also assumed the internal velocity dispersion ($\equiv \sigma$) to be 1.0 km s^{-1} (Stark et al. 2004). On these assumptions, we made model P-V diagrams with different central masses, and the model P-V diagram in Figure 7 shows that the compact high-velocity emission could be interpreted as an infalling disk onto the central stellar mass of $\sim 1 \text{ M}_\odot$ with an acceptable mass range from $\sim 0.5 \text{ M}_\odot$ to $\sim 2.0 \text{ M}_\odot$. An uncertainty of $\pm 10^\circ$ of the inclination angle of the flattened structure could reproduce additional $\sim 20\%$ uncertainty of the central mass. From VLBI studies of H_2O masers in I16293, Imai et al.

(1999) have found a rotating-infalling disk with an outer radius of 100 AU around Source A. Their estimates of the inclination angle and the central stellar mass are $\sim 35^\circ$ and $\sim 0.3 M_\odot$, respectively. These estimates are roughly consistent with our estimates ($\sim 57^\circ$, and $\sim 1.0 M_\odot$), and the compact HCN structure detected with our observations can be interpreted as tracing the outer part of the same infalling disk.

From the optically-thin HC¹⁵N emission, we estimated the mass of the compact structure within the radius of ~ 230 AU ($\equiv r$) to be $0.084 M_\odot$ ($\equiv M_r$). Here, we assume the HC¹⁵N emission to be optically thin, the excitation temperature to be 30 (K) (Schöier et al. 2002), and the HC¹⁵N abundance to be 7.4×10^{-11} (Kuan et al. 2004). The infalling velocity at that radius is 2.8 km s^{-1} ($\equiv v_r$) from our model. Then, the mass accretion rate ($\equiv \dot{M}$) can be estimated from

$$\dot{M} = M_r v_r / r \quad (2)$$

and we find a value of $2.2 \times 10^{-4} (M_\odot \text{ year}^{-1})$. This value of the mass accretion rate is 4 times higher than that estimated by Schöier et al. (2002) ($\sim 5 \times 10^{-5} M_\odot \text{ year}^{-1}$). Schöier et al. 2002 assumed that the entire (~ 3000 AU in size) circumbinary envelope is infalling and derived the mass accretion rate from a model fitting to their JCMT spectra. On the other hand, from our higher spatial-resolution observations we suggest that only the compact HCN/HC¹⁵N component associated with Source A is infalling, and we derived the mass accretion rate in the compact HCN component from our toy model. The difference of the estimated mass accretion rate probably arises from the different configuration adopted. From the estimated mass accretion rate, the accretion luminosity ($\equiv L_{acc}$) can be calculated as

$$L_{acc} = \frac{GM_* \dot{M}}{R_*} \quad (3)$$

where G is a gravitational constant, M_* is a mass of the central protostar, and R_* is a radius of the central protostar. If we assume $R_* = 4 R_\odot$ (Stahler et al. 1980), L_{acc} is estimated to be $\sim 1600 L_\odot$ with our \dot{M} value and to be $\sim 390 L_\odot$ with the \dot{M} value by Schöier et al. (2002). These values are much higher than the bolometric luminosity of I16293 ($= 27 L_\odot$; Walker et al. 1986), so that the so-called “luminosity problem” (Kenyon et al. 1990) discussed by Ohashi et al. (1996) and Saito et al. (1996) for L1551 IRS5 also exists in I16293. The reason of this discrepancy is still unclear. One possible explanation is that the infalling motion found in the present study is not onto the surface of the protostar itself, but onto the central rotationally-supported disk around the protostar. Here, the radius of the

terminal point in the gravitational potential is likely to be much larger than that adopted in the above estimates. If we assume the radius of the terminal point to be ~ 1 AU, our estimated mass infalling rate is consistent with the bolometric luminosity. Another possible explanation is that the accretion may be non-steady.

We note that an infalling motion has the same radial dependence as that of a Keplerian rotation ($\propto r^{-0.5}$), and that they are indistinguishable from the examination of the P-V diagram alone. The only clue to distinguish the two motions is the disk orientation as compared to the direction of the velocity gradient. In fact, Huang et al. (2005) have interpreted the velocity gradient in the HC^{15}N emission as a Keplerian rotation around Source A. However, the position angle of the flattened structure in the optically-thin line (-16°) as well as that of the inner rotating-infalling disk traced by the H_2O maser (Imai et al. 1999), seems to favor the interpretation of the infalling motion. Furthermore, the interpretation of the Keplerian rotation implies that there is a well-developed 500 AU scale rotationally-supported disk around the Class 0 protostar with the significant molecular outflows. In general, such well-developed large-scale (~ 500 AU) Keplerian disks are observed around more evolved sources, that is, Class II sources, as in the case of a circumbinary Keplerian ring around GG Tau (Guilloteau et al. 1999) and a Keplerian protoplanetary disk around DM Tau (Guilloteau & Dutrey 1998). From these considerations, we suggest that the infall gas motion is a more appropriate interpretation than that of the Keplerian rotation.

The SMA+JCMT P-V diagram in Figure 7 exhibits another lower-velocity, extended component as seen in the velocity channel maps of Figure 4, which is mostly filtered out by the interferometer alone. The velocity structure in this extended lower-velocity component is clearly different from that in the compact high-velocity component; the velocity increases further from Source A. Since the cut of the P-V diagram is approximately parallel to the axis of the associated CO outflow (see Figure 6) and this type of velocity gradients is expected in molecular outflows driven by the wide-angle wind, we suggest that this extended HCN emission arises from turbulent gas swept up by the associated outflow from Source A. Our simple thin-layer model with the Gaussian intensity distribution shown in the right panel of Figure 7 is consistent with the interpretation that this low-velocity component could be an outflowing gas perpendicular to the compact high-velocity structure.

In Figure 8, we show P-V diagrams along the cut through Source A and B (P.A. = 138.8°) in the HCN emission with the SMA-only (gray) and SMA+JCMT (black contour), and in the HC^{15}N emission with the SMA (red contour). At the position of Source A the wide velocity width in the HCN and HC^{15}N high-velocity component is evident. At the position of Source B, a weak HC^{15}N component with a narrow line width ($\sim 2 \text{ km s}^{-1}$) is seen, which is smeared out in the total integrated intensity map of Figure 3 and embedded in the extended

HCN emission. This component at Source B is most likely a molecular structure found by the previous SMA observations (Kuan et al. 2004; Chandler et al. 2005), as well as that by the previous Plateau de Bure observations (Bottinelli et al. 2004). In Figure 8, there is also an extended structure with narrow line width, which is likely to be the extended ambient gas.

4.2. Different Evolution of the Binary Protostars ?

Our submillimeter HCN and HC^{15}N observations of I16293 show that an intense compact (~ 500 AU) molecular component with a wide velocity width ($> 10 \text{ km s}^{-1}$) is associated with Source A but only a weak molecular component with a narrow velocity width ($\sim 2 \text{ km s}^{-1}$) is associated with Source B. SMA observations of I16293 in the CO (2–1, 3–2) lines have revealed that Source A is clearly driving molecular outflows, and that there is no clear outflow activity from Source B (Yeh et al. 2007). Source A is associated with a number of hot core tracers such as complex organic molecules that are less prominent or not present at Source B (Kuan et al. 2004; Chandler et al. 2005). These results imply that Source A and B are at different evolutionary stages in the common circumbinary envelope, although it is unclear which source is younger. In terms of protostellar activity traced by molecular lines, Source A seems to be younger than Source B, since Source A has substantial surrounding molecular gas and clear outflow emission, and shows a number of hot core tracers (Kuan et al. 2004; Chandler et al. 2005), while Source B is more like a T Tauri star without a significant gas component or CO outflow. On the other hand, if the compactness in the continuum emission represents younger evolutionary stage of the circumstellar disk, Source B may be younger than Source A as suggested by Rodríguez et al. (2005) and Chandler et al (2005). In fact, Chandler et al (2005) have found redshifted SO (7₇–6₆) absorption against the strong continuum emission at Source B, which they suggest is the unambiguous detection of infall toward the central protostar.

There are other examples of binary protostars where the components exhibit different observational characteristics that suggests they are in different evolutionary stages. Bourke (2001) has found two 7 μm sources with a separation of ~ 3400 AU in BHR 71 with the Infrared Space Observatory. The brighter companion (IRS 1) is associated with the millimeter continuum source (BHR 71 mm) while the other weaker companion (IRS 2) is not, and IRS 1 drives a powerful molecular outflow while IRS 2 drives a much less massive outflow. From these results, it is suggested that IRS1 and IRS2 in BHR 71 is a protobinary system at different evolutionary stages, and that IRS 2 is more evolved than IRS 1. High angular-resolution ($\sim 2''$) observations of CB 230 show compact millimeter emission associated with

only one component of an NIR protostellar pair separated by $\sim 10''$, suggesting that like BHR 71 only this component has a substantial circumstellar disk, although both protostars in CB 230 drive CO outflows (Launhardt 2001). A similar example is also seen in the SVS 13 close binary system (separation ~ 65 AU). Anglada et al. (2004) reported from their high-resolution 7-mm observations with VLA that only one of the components of the SVS 13 system (VLA 4B) is associated with detectable circumstellar dust emission, while the other component is optically visible without significant dust emission. These recent observational results indicate that members of protostellar binary systems can exist at different evolutionary stages.

Theoretically it is not clear how to form binary companions at different evolutionary stages in the common envelope and this idea remains controversial. According to recent theoretical models of binary formation in this common envelope type (Nakamura & Li 2003), fragmentation of “the first bar” which was made through the contraction of the envelope produces binary or multiple stars, but the stellar age must be the same. Subsequent merging of the fragments may be necessary to make binary companions at different evolutionary stages. Ochi et al. (2005) have conducted high-resolution numerical simulations of an accretion from a circumbinary envelope onto the primary and secondary of the binary companion. Their simulations suggest that the accretion rate of the primary is larger than that of the secondary, regardless of the specific angular momentum of the accreting gas, and that the gas accretion tends to increase the mass difference between the primary and secondary. Their results are qualitatively different from earlier works by Bate & Bonnell (1997), which suggests that the primary accretes more than the secondary only when the accreting gas has a low specific angular momentum. More theoretical works, as well as an accumulation of observational data, are required to address this issue.

5. Conclusions

We have carried out submillimeter interferometric and single-dish observations of the well-known protobinary system IRAS 16293-2422 with the SMA in the HCN (4–3) and HC¹⁵N (4–3) lines, in the continuum at 354.5 GHz and with the JCMT in the HCN (4–3) line. These data have provided us with the following results;

1. The 354.5 GHz continuum observations with the SMA resolve the individual binary companions (Source A and Source B). The dust emission at Source A is elongated along the North-East to South-West direction (300×150 AU; P.A. = 33°), while that at Source B is more compact (150×140 AU). The elongation at Source A is likely to reflect the presence of the close binary system (Aa and Ab). The integrated submillimeter flux in both sources

is ~ 4.0 Jy.

2. The optically-thin HC^{15}N (4–3) emission reveals a compact (~ 500 AU) flattened structure (P.A. = -16°) associated with Source A. There is a clear velocity gradient in this compact structure along the East (Blue) to West (Red) direction, which can be interpreted as an infalling gas motion in the flattened structure onto Source A with a central mass of $\sim 1 M_\odot$ and an inclination angle of $\sim 57^\circ$ from the plane of the sky. The combined HCN image shows an extended (~ 3000 AU) circumbinary envelope as well as the compact structure associated with Source A. In the extended circumbinary envelope there is also a low-velocity North-East (Blue) to South-West (Red) gradient, which may be due to gas swept up by the outflow.

3. Contrary to Source A, at Source B there is only a weak molecular component with a much narrower line width ($\sim 2 \text{ km s}^{-1}$), and no clear outflow activity. These results, together with the fewer number of complex molecules associated with Source B (Kuan et al. 2004; Chandler et al. 2005), may suggest different evolutionary stages between Source A and B in the common circumbinary envelope. With the data presented we are unable to determine whether Source B is younger or older.

We are grateful to R. Kawabe, E. F. van Dishoeck, and P. C. Myers for fruitful discussions. We also acknowledge T. Hanawa and F. Nakamura for their comments on theoretical studies of binary formations. We would like to thank all the SMA staff supporting this work. S.T. and T.B. were supported by a postdoctoral fellowship of the Smithsonian Astrophysical Observatory. The research of Y.-J. K. was supported by NSC 94-2112-M-003-010.

A. Combining SMA and JCMT Data

The procedure adopted to combine the SMA and JCMT data is similar to that described by Takakuwa et al. (2003a), which is based on the description for combining single-dish and interferometric data by Vogel et al. (1984), and on the MIRIAD scripts developed by Wilner & Welch (1994). We first re-sampled the JCMT image cube along the velocity axis to match the velocity channels with that of the SMA visibility. Next, we deconvolved the JCMT image by the $15''$ Gaussian image which represents the JCMT beam. Then, we multiplied the JCMT image with the $35''$ Gaussian image which is intended to approximate the SMA primary beam, that is, inverse of the primary beam correction. In these beam corrections we ignore any effect of sidelobes of the JCMT and SMA beam, which are not well-known. From the resultant JCMT image cube we made JCMT visibility data which fill in the central hole of the SMA *uv*-track by the MIRIAD task *uvrandom* and *uvmodel*. The single-dish

sampling in the uv plane was chosen so that the number of the uv data points per unit uv distance is similar to that of the SMA data ($= 40$ uv data points per $1k\lambda$). We checked that the JCMT amplitude is approximately consistent with the SMA amplitude.

The JCMT visibility data were Fourier-transformed along with the SMA visibility data to make a combined image cube by the MIRIAD task *invert*. We adopted $\text{robust} = 0.5$ weighting for the imaging, which seems to provide a good compromise between the spatial resolution and the noise level. The resultant synthesized beam size and the rms noise level is $1''.3 \times 1''.2$ (P.A. = 30°) and ~ 0.90 Jy beam $^{-1}$ channel $^{-1}$, respectively. Negative sidelobes in the SMA synthesized beam are significantly suppressed in the combined beam. The final combined image with the JCMT and SMA has a high spatial dynamic range from large-scale (~ 3000 AU) to small scale (~ 200 AU) without any effect of missing flux. In Figure 9, we compare the JCMT, SMA, and combined images of I16293 in the HCN emission. The JCMT image shows a 3000 AU-scale circular blob and western elongation centered at Source A without any fine-scale structure. In the SMA image, finer structures are picked up but extended gas components are mostly resolved out. In the combined image, both extended and compact structures are successfully sampled.

B. Importance of Combining Single-Dish and Interferometric Data

Our combined SMA+JCMT observations of I16293 in the submillimeter HCN emission have revealed that the submillimeter emission extends more than ~ 3000 AU in I16293. This extent cannot be recovered with the SMA, since the minimum projected uv distance of the SMA observations was $\sim 10.0 k\lambda$ and the SMA observations were insensitive to structures more extended than ~ 2600 AU at 10% level (Wilner & Welch 1994). In fact, our SMA observations recovered only $\sim 35\%$ of the total JCMT flux toward Source A. For comparison, SMA observations of L1551 IRS5, another low-mass protostellar envelope, recovered only $\sim 11\%$ of the total submillimeter CS (7–6) flux, which suggests that there is > 1500 AU-scale extended submillimeter emission in L1551 IRS5 (Takakuwa et al. 2004).

The rotational energy level of the upper state is 43 K and 66 K in HCN (4–3) and CS (7–6), and the critical density $\geq 10^8$ cm $^{-3}$ and $\geq 10^7$ cm $^{-3}$, respectively. These temperatures and gas densities are much higher than those traced by millimeter-wave tracers, such as C 18 O ($J=1-0$) (5 K and $\sim 10^4$ cm $^{-3}$; Sargent et al. 1988, Momose et al. 1998) or H 13 CO $^+$ ($J=1-0$) (4 K and $\sim 10^5$ cm $^{-3}$; Saito et al. 2001). It is puzzling why those submillimeter molecular lines which trace such warmer and denser gas can be so extended. It seems to be difficult to make gas temperature high enough only by the heating from central stars (e.g., Lay et al. 1994). As discussed in §4.1, there is significant contamination from the associated

outflows in the submillimeter HCN emission, and the interaction between the circumbinary envelope and the outflowing gas could be a source of such extended submillimeter emission (Avery & Chiao 1996; Nakamura 2000). To sample those extended submillimeter emission lines and to study the structure and kinematics from protostellar envelopes (> 1500 AU) to compact circumstellar disks (≤ 200 AU) unambiguously, it is quite important to make both submillimeter single-dish and interferometric observations and to combine the two data sets.

REFERENCES

- Anglada, G., Rodríguez, L. F., Osorio, M., Torrelles, J. M., Estalella, R., Beltrán, M. T., & Ho, P. T. P. 2004, *ApJ*, 605, L137
- Avery, L. W. & Chiao, M. 1996, *ApJ*, 463, 642
- Bate, M. R., & Bonnell, I. A., 1997, *MNRAS*, 285, 33
- Beckwith, S. V. W., & Sargent, A. I. 1996, *Nature*, 383, 139
- Benson, P. J., & Myers, P. C. 1989, *ApJS*, 71, 89
- Beltrán, M. T., Girart, J. M., Estalella, R., & Ho, P. T. P. 2004, *A&A*, 426, 941
- Blake, G. A., van Dishoeck, E. F., Jansen, D. J., Groesbeck, T. D., & Mundy, L. G. 1994, *ApJ*, 428, 680
- Blake, G. A., Sandell, G., van Dishoeck, E. F., Groesbeck, T. D., Mundy, L. G., & Aspin, C. 1995, *ApJ*, 441, 689
- Bottinelli, S., Ceccarelli, C., Neri, R., Williams, J. P., Caux, E., Cazaux, S., Lefloch, B., Maret, S., & Tielens, A. G. G. M. 2004, *ApJ*, 617, L69
- Bourke, T. L. 2001, *ApJ*, 554, L91
- Bourke, T. L., Crapsi, A., Myers, P. C., Evans II, N. J., Wilner, D. J., Huard, T. L., Jørgensen, J. K., & Young, C. H. 2005, *ApJ*, 633, L129
- Castets, A., Ceccarelli, C., Loinard, L., Caux, E., & Lefloch, B. 2001, *A&A*, 375, 40
- Cazaux, S., Tielens, A. G. G. M., Ceccarelli, C., Castets, A., Wakelam, V., Caux, E., Parise, B., & Teyssier, D. 2003, *ApJ*, 593, L51
- Ceccarelli, C., Castets, A., Caux, E., Hollenbach, D., Loinard, L., Molinari, S., & Tielens, A. G. G. M. 2000a, *A&A*, 355, 1129

- Ceccarelli, C., Loinard, L., Castets, A., Tielens, A. G. G. M., & Caux, E. 2000b, *A&A*, 357, L9
- Chandler, C. J., Brogan, C. L., Shirley, Y. L., & Loinard, L. 2005, *ApJ*, 632, 371
- Choi, M., Panis, J.-F., & Evans II, N. J., 1999, *ApJS*, 122, 519
- de Geus, E. J., de Zeeuw, P. T., & Lub, J. 1989, *A&A*, 216, 44
- Di Francesco, J., Myers, P. C., Wilner, D. J., Ohashi, N., & Mardones, D. 2001, *ApJ*, 562, 770
- Evans II, N. J., Lee, J.-E., Rawlings, J. M. C., & Choi, M. 2005, *ApJ*, 626, 919
- Fuller, G. A., & Wootten, A. 2000, *ApJ*, 534, 854
- Garay, G., Mardones, D., Rodríguez, L. F., Caselli, P., & Bourke, T. L. 2002, *ApJ*, 567, 980
- Gueth, F., Guilloteau, S., & Bachiller, R. 1996, *A&A*, 307, 891
- Guilloteau, S., & Dutrey, A. 1998, *A&A*, 339, 467
- Guilloteau, S., Dutrey, A., & Simon, M. 1999, *A&A*, 348, 570
- Hayashi, M., Ohashi, N., & Miyama, S. M. 1993, *ApJ*, 418, L71
- Hirano, N., Mikami, H., Umemoto, T., Yamamoto, S., & Taniguchi, Y. 2001, *ApJ*, 547, 899
- Ho, P. T. P., Moran, J. M., & Lo, K. Y. 2004, *ApJ*, 616, L1
- Hogerheijde, M. R., van Dishoeck, E. F., Blake, G. A., & van Langevelde, H. J. 1997, *ApJ*, 489, 293
- Hogerheijde, M. R., van Dishoeck, E. F., Salverda, J. M., & Blake, G. A. 1999, *ApJ*, 513, 350
- Hogerheijde, M. R. 2001, *ApJ*, 553, 618
- Huang, H.-C., Kuan, Y.-J., Charnley, S. B., Hirano, N., Takakuwa, S., & Bourke, T. L. 2005, *Adv. in Space Sci.*, 36, 146
- Imai, H., Iwata, T., & Miyoshi, M. 1999, *PASJ*, 51, 473
- Jørgensen, J. K., Bourke, T. L., Myers, P. C., Schöier, F. L., van Dishoeck, E. F., & Wilner D. J. 2005, *ApJ*, 631, L77

- Kenyon, S. J., Hartmann, L. W., Strom, K. M., & Strom, S. E. 1990, AJ, 99, 869
- Knude, J. & Høg, E. 1998, A&A, 338, 897
- Kuan, Y.-J., Huang, H.-C., Charnley, S. B., Hirano, N., Takakuwa, S., Wilner, D. J., Liu, S.-Y., Ohashi, N., Bourke, T. L., Qi, C., & Zhang, Q. 2004, ApJ, 616, L27
- Larson, R. B. 1969, MNRAS, 145, 271
- Launhardt, R. 2001, in IAU Symp. 200, The Formation of Binary Stars, ed. H. Zinnecker & R. D. Mathieu (San Francisco: ASP), 117
- Lay, O. P., Carlstrom, J. E., Hills, R. E., & Phillips, T. G. 1994, ApJ, 434, L75
- Looney, L. W., Mundy, L. G., & Welch, W. J. 2000, ApJ, 529, 477
- Lucas, R., & Liszt, H. 1998, A&A, 337, 246
- Masunaga, H., & Inutsuka, S. 2000, ApJ, 536, 406
- Menten, K. M., Serabyn, E., Guesten, R., & Wilson, T. L. 1987, A&A, 177, L57
- Mizuno, A., Fukui, Y., Iwata, T., Nozawa, S., & Takano, T. 1990, ApJ, 356, 184
- Momose, M., Ohashi, N., Kawabe, R., Nakano, T., & Hayashi, M. 1998, ApJ, 504, 314
- Mundy, L. G., Wootten, H. A., & Wilking, B. A. 1990, ApJ, 352, 159
- Mundy, L. G., Wootten, A., Wilking, B. A., Blake, G. A., & Sargent, A. I. 1992, ApJ, 385, 306
- Myers, P. C., Bachiller, R., Caselli, P., Fuller, G. A., Mardones, D., Tafalla, M., & Wilner, D. J. 1995, ApJ, 449, L65
- Nakamura, F. 2000, ApJ, 543, 291
- Nakamura, F., & Li, Z.-Y. 2003, ApJ, 594, 363
- Narayanan, G., Walker, C. K., & Buckley, H. D. 1998, ApJ, 496, 292
- Ochi, Y., Sugimoto, K., & Hanawa, T. 2005, ApJ, 623, 922
- Ohashi, N., Hayashi, M., Ho, P. T. P., Momose, M., & Hirano, N. 1996, ApJ, 466, 957
- Ohashi, N., Hayashi, M., Ho, P. T. P., & Momose, M. 1997a, ApJ, 475, 211

- Ohashi, N., Hayashi, M., Ho, P. T. P., Momose, M., Tamura, M., Hirano, N., & Sargent, A. I. 1997b, *ApJ*, 488, 317
- Penston, M. V. 1969, *MNRAS*, 144, 425
- Rodríguez, L. F., Loinard, L., D'Alessio, P., Wilner, D. J., & Ho, P. T. P. 2005, *ApJ*, 621, L133
- Saito, M., Kawabe, R., Kitamura, Y., & Sunada, K. 1996, *ApJ*, 473, 464
- Saito, M., Kawabe, R., Kitamura, Y., & Sunada, K. 2001, *ApJ*, 547, 840
- Sargent, A. I., Beckwith, S., Keene, J., & Masson, C. 1988, *ApJ*, 333, 936
- Sault, R. J., Teuben, P. J., & Wright, M. C. H. 1995, *Astronomical Data Analysis Software and Systems IV*, ASP Conference Series, Vol. 77, R. A. Shaw, H. E. Payne, & J. J. E. Hayes, eds., p.433
- Schöier, F. L., Jørgensen, J. K., van Dishoeck, E. F., & Blake, G. A. 2002, *A&A*, 390, 1001
- Schöier, F. L., Jørgensen, J. K., van Dishoeck, E. F., & Blake, G. A. 2004, *A&A*, 418, 185
- Scoville, N. Z., Carlstrom, J. E., Chandler, C. J., Phillips, J. A., Scott, S. L., Tilanus, R. P. J., & Wang, Z. 1993, *PASP*, 105, 1482
- Stahler, S. W., Shu, F. H., & Taam, R. E. 1980, *ApJ*, 241, 637
- Stark, R., Sandell, G., Beck, S. C., Hogerheijde, M. R., van Dishoeck, E. F., van der Wal, P., van der Tak, F. F. S., Schäfer, F., Melnick, G. J., Ashby, M. L. N., & de Lange, G. 2004, *ApJ*, 608, 341
- Takahashi, S., Saito, M., Takakuwa, S., & Kawabe, R. 2006, *ApJ*, 651, 933
- Takakuwa, S., Mikami, H., Saito, M., & Hirano, N. 2000, *ApJ*, 542, 367
- Takakuwa, S., Kamazaki, T., Saito, M., & Hirano, N. 2003a, *ApJ*, 584, 818
- Takakuwa, S., Ohashi, N., & Hirano, N. 2003b, *ApJ*, 590, 932
- Takakuwa, S., Ohashi, N., Ho, P. T. P., Chunhua, Q., Wilner, D. J., Qizhou, Z., Bourke, T. L., Hirano, N., Choi, M., & Yang, J. 2004, *ApJ*, 616, L15
- Terebey, S., Chandler, C. J., & André 1993, *ApJ*, 414, 759
- van Dishoeck, E. F., Blake, G. A., Jansen, D. J., & Groesbeck, T. D. 1995, *ApJ*, 447, 760

- Vogel, S. N., Wright, M. C. H., Plambeck, R. L., & Welch, W. J. 1984, *ApJ*, 283, 655
- Walker, C. K., Lada, C. J., Young, E. T., Maloney, P. R., & Wilking, B. A. 1986, *ApJ*, 309, L47
- Walker, C. K., Lada, C. J., Young, E. T., & Margulis, M. 1988, *ApJ*, 332, 335
- Welch, W. J., Hartmann, L., Helfer, T., & Briceño, C. 2000, *ApJ*, 540, 362
- Whittet, D. C. B. 1974, *MNRAS*, 168, 371
- Wilner, D. J., & Welch, W. J. 1994, *ApJ*, 427, 898
- Wootten, A. 1989, *ApJ*, 337, 858
- Yeh, S. C. C., et al. 2007, *ApJ*, submitted
- Zhou, S., Yuefang, W., Evans II, N. J., Fuller, G. A., & Myers, P. C. 1989, *ApJ*, 346, 168
- Zhou, S. 1992, *ApJ*, 394, 204
- Zhou, S., Evans, N. J., II, Wang, Y., Peng, R., & Lo, K. Y. 1994, *ApJ*, 433, 131
- Zhou, S. 1995, *ApJ*, 442, 685

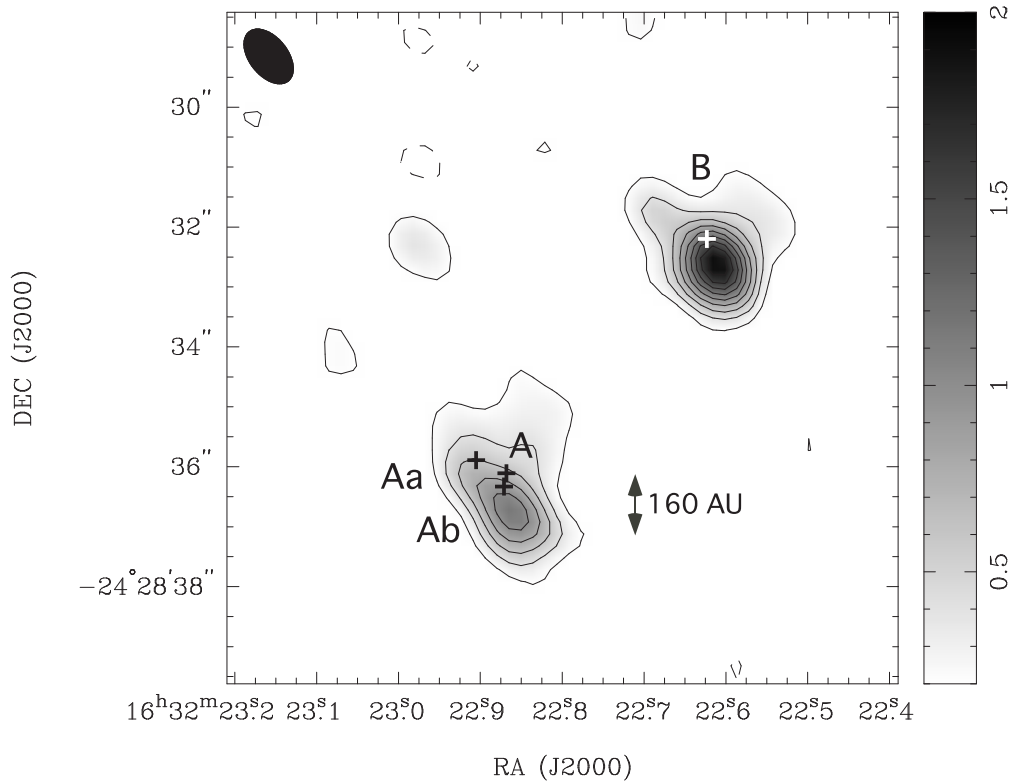


Fig. 1.— 354.5 GHz continuum image in I16293 taken with the SMA. Contour levels are from 3σ in steps of 3σ ($1\sigma = 0.066$ Jy beam $^{-1}$). The synthesized beam size, shown at the top left corner of the panel, is $1''.05 \times 0''.64$ (P.A. = 38.6°) with the uniform weighting. Crosses with the label “A” and “B” indicate positions of the 2.7-mm continuum peak observed with BIMA (Looney, Mundy, & Welch 2000), and those with the label “Aa” and “Ab” positions of the 300 GHz continuum peaks observed by Chandler et al. (2005). The size of the crosses shows the astrometric accuracy of the BIMA data.

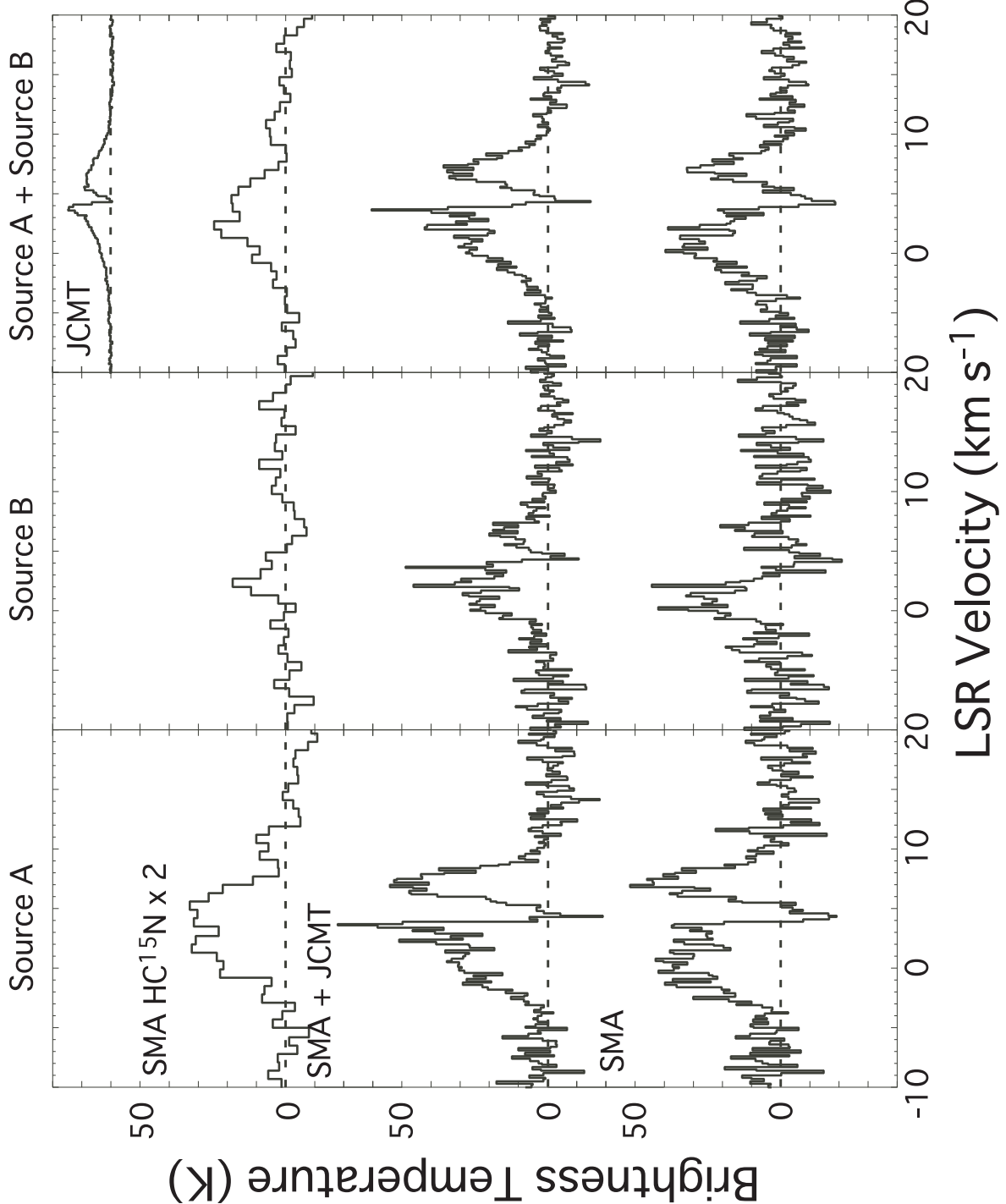


Fig. 2.— HCN (4-3) line profiles toward Source A (left) and Source B (middle) taken with the SMA (bottom) and SMA + JCMT (middle), and HC¹⁵N (4-3) line profiles taken with the SMA (top). For comparison with the JCMT HCN (4-3) spectrum, we also plot the average spectra toward Source A and Source B (right). The spatial resolution of the HCN spectra is $1.^{\prime\prime}3 \times 1.^{\prime\prime}2$ (P.A. = 30°). The spatial resolution of the JCMT spectra is $15''$, and that of the SMA HC¹⁵N spectra $1.^{\prime\prime}6 \times 1.^{\prime\prime}3$ (P.A. = 14°). The rms noise level of the JCMT, SMA, and the combined spectra is 0.13 K, 7.4 K, and 5.6 K, respectively.

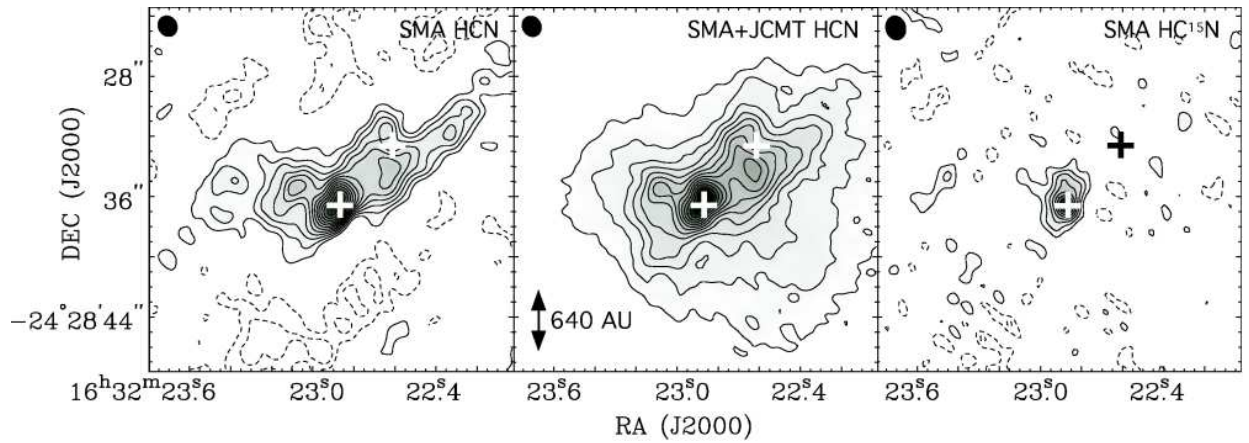


Fig. 3.— Total integrated intensity maps in I16293 taken with the SMA (left) and SMA+JCMT (middle) in the HCN (4-3) emission, and the HC¹⁵N (4-3) emission with the SMA (right). Crosses in each panel indicate positions of the 354.5 GHz continuum emission observed with the SMA (Fig.1, Table 2). Filled ellipses at the top left corner of each panel show the synthesized beam, that is, $1.^{\prime\prime}3 \times 1.^{\prime\prime}2$ (P.A. = 30°) in the SMA and the combined map, and $1.^{\prime\prime}6 \times 1.^{\prime\prime}3$ (P.A. = 14°) in the SMA HC¹⁵N map. Contour levels are from 33.50 K km s⁻¹ in steps of 22.33 K km s⁻¹ in the SMA and combined HCN map (3σ in steps of 2σ in the SMA HCN map), and from 3σ in steps of 2σ ($1\sigma = 6.49$ K km s⁻¹) in the SMA HC¹⁵N map.

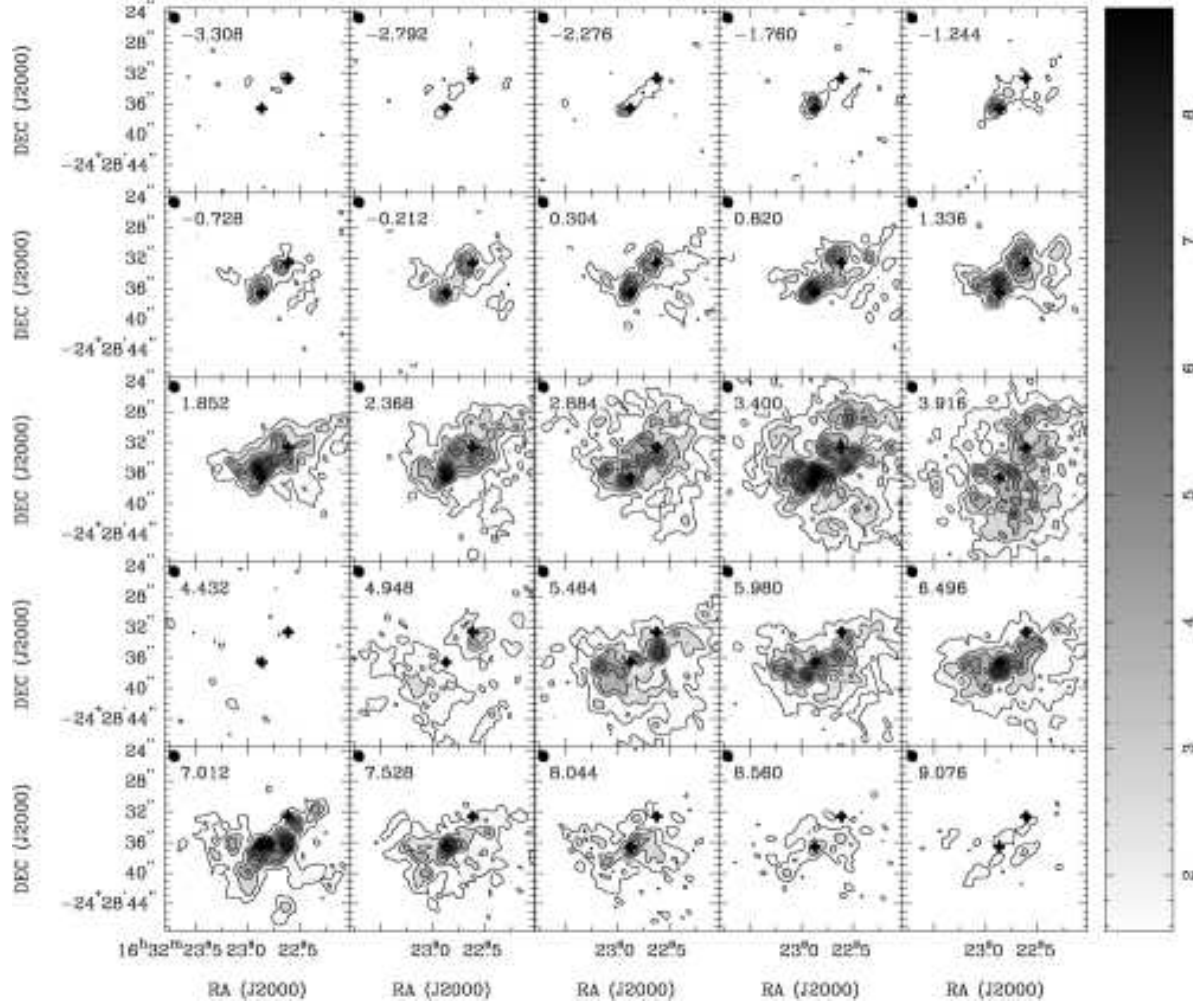


Fig. 4.— SMA + JCMT velocity channel maps of I16293 in the HCN (4–3) line. Each panel is an average of 3 channels (1 channel = 0.172 km s^{-1}). Crosses in each panel indicate positions of the 354.5 GHz continuum emission observed with the SMA (Fig.1, Table 2). The synthesized beam size is shown as a filled ellipse at the top left corner of each panel. Numbers at the upper-left corner of each panel are V_{LSR} (km s^{-1}). Contour levels are from 2σ in steps of 2σ ($1\sigma = 3.23 \text{ K}$).

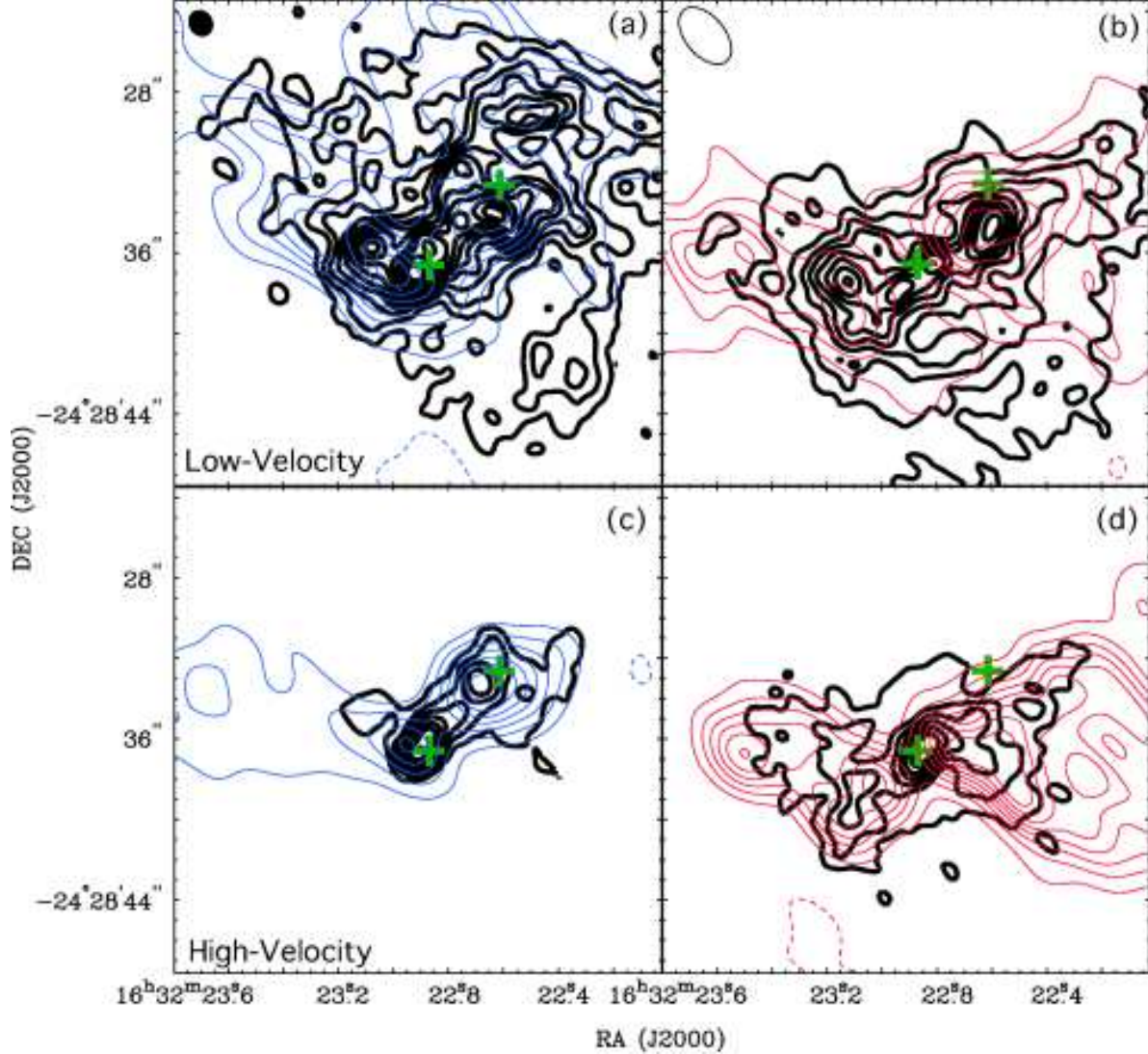


Fig. 5.— SMA + JCMT velocity channel maps of I16293 in the HCN (4-3) emission at four different velocity ranges: (a) low-velocity blueshifted range ($2.54 - 3.40 \text{ km s}^{-1}$); (b) low-velocity redshifted range ($4.95 - 6.50 \text{ km s}^{-1}$); (c) high-velocity blueshifted range ($-2.62 - +0.65 \text{ km s}^{-1}$); and (d) high-velocity redshifted range ($7.36 - 9.08 \text{ km s}^{-1}$), superposed on the CO (2-1) outflow map taken with the SMA (blue and red contours; Yeh et al. 2007). Contour levels are from 5.30 (K) in steps of 3.54 (K) in the HCN map and 5.68 (K) in steps of 5.68 (K) in the CO map. Green crosses indicate positions of the protobinary (Fig. 1, Table 2). A filled ellipse at the top left corner of panel (a) indicates the synthesized beam of the HCN observations ($1''.3 \times 1''.2$; P.A. = 30°), while an open ellipse at the top left corner of panel (b) the synthesized beam size of the CO map ($3''.3 \times 2''.0$; P.A. = 40°).

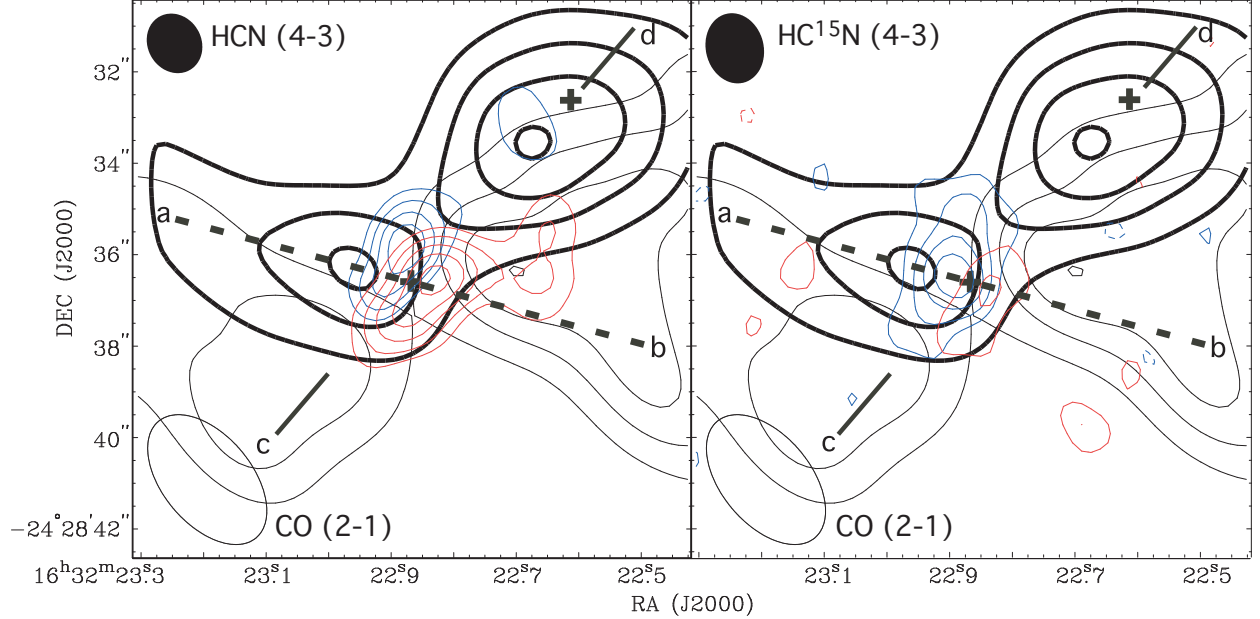


Fig. 6.— High-velocity blueshifted ($V_{LSR} = -2.62 - 2.37 \text{ km s}^{-1}$) and redshifted ($V_{LSR} = 5.98 - 9.08 \text{ km s}^{-1}$) HCN (4–3) emission taken with the SMA and JCMT (left) and HC¹⁵N (4–3) emission taken with the SMA (right) in I16293. The velocity range is set to be wider than that of Figure 5 in order to improve the signal-to-noise ratio of the HC¹⁵N image. The CO (2–1) outflow map taken with the SMA (Yeh et al. 2007) is overlaid on the HCN and HC¹⁵N images. The blueshifted and redshifted components in the HCN and HC¹⁵N lines are shown in blue and red contours, while the blueshifted and redshifted CO outflow in black bold and thin contours, respectively. Contour levels are from 19.4 (K) in steps of 3.5 (K) in the HCN map, from 3.2 (K) in steps of 2.1 (K) in the HC¹⁵N map, and from 17.1 K in steps of 11.4 K in the CO map. Crosses indicate positions of the 354.5 GHz continuum emission observed with the SMA (Fig. 1, Table 2). A filled ellipse at the top left corner shows the synthesized beam of the HCN ($1.^{\circ}3 \times 1.^{\circ}2$; P.A. = 30°) and HC¹⁵N ($1.^{\circ}6 \times 1.^{\circ}3$; P.A. = 14°) images, while open ellipses at the bottom left corner the synthesized beam of the CO (2–1) image ($3.^{\circ}3 \times 2.^{\circ}0$; P.A. = 40°). Lines a-b and c-d indicate cuts of the Position-Velocity diagrams shown in Figure 7 and 8, respectively.

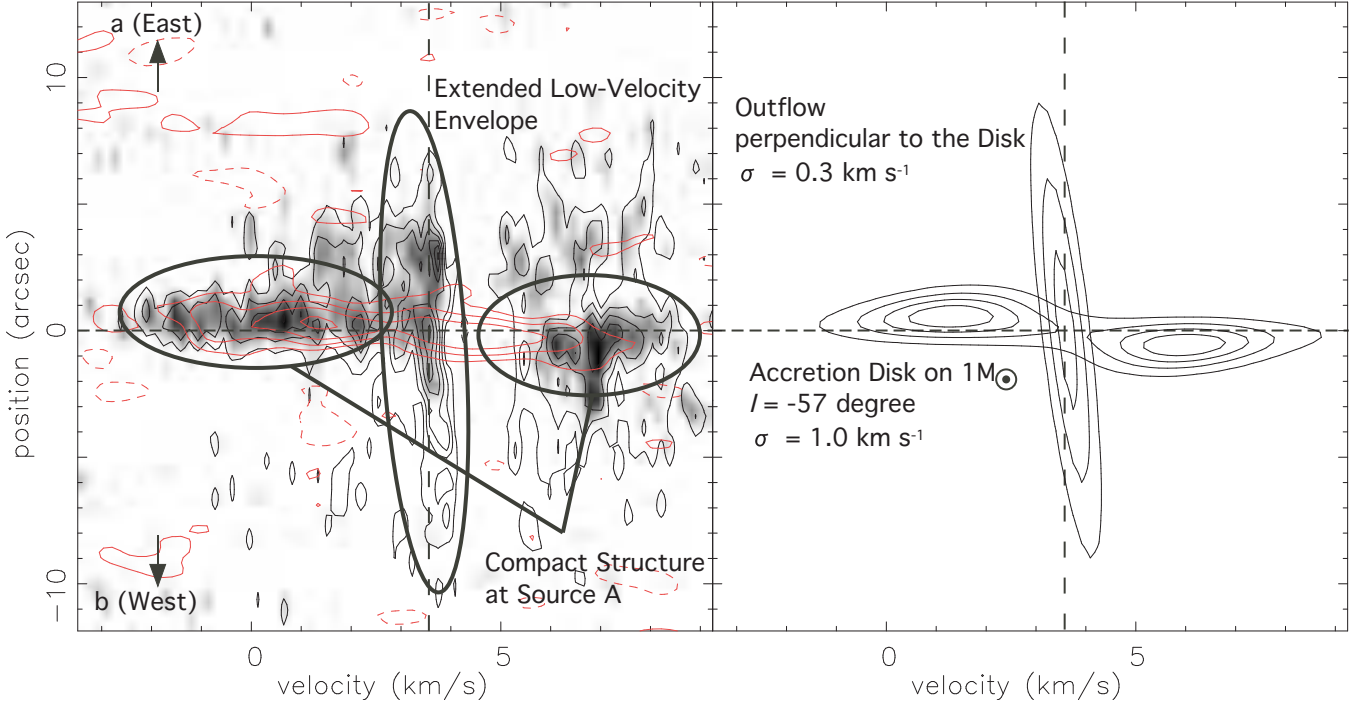


Fig. 7.— Left: Position-Velocity (P-V) diagrams along the minor axis of the compact flattened structure at Source A in the HC^{15}N (4-3) emission (red contour; P.A. = 74°), as well as in the HCN (4-3) line with the SMA + JCMT (black contour) and SMA (gray). Contour levels are from 11.2 (K) in steps of 11.2 (K) in the HCN emission and from 4.23 (K) in steps of 4.23 (K) in the HC^{15}N emission. A horizontal dashed line indicates the position of Source A, and a vertical dashed line the systemic velocity ($\sim 3.6 \text{ km s}^{-1}$). There are two distinct components, one is the high-velocity compact structure seen in the SMA HCN and HC^{15}N images and the other the extended low-velocity envelope seen in the combined image. Right: Model P-V diagrams to interpret the observational P-V diagrams in the left panel. Contour levels are the same as in the combined HCN P-V diagram. The P-V diagram of the high-velocity compact structure can be interpreted as an accretion motion onto the central mass of $1 M_{\odot}$ in the geometrically thin disk with an inclination angle of 57° from the plane of the sky and an internal velocity dispersion ($\equiv \sigma$) of 1.0 km s^{-1} . The P-V diagram of the extended component can be understood as an outflowing gas perpendicular to the flattened structure with an internal velocity dispersion of 0.3 km s^{-1} . The model emission is assumed to have Gaussian intensity distribution. The strong self-absorption around $V_{LSR} = 4 - 5 \text{ km s}^{-1}$ seen in the real data can not be reproduced with this “toy” model.

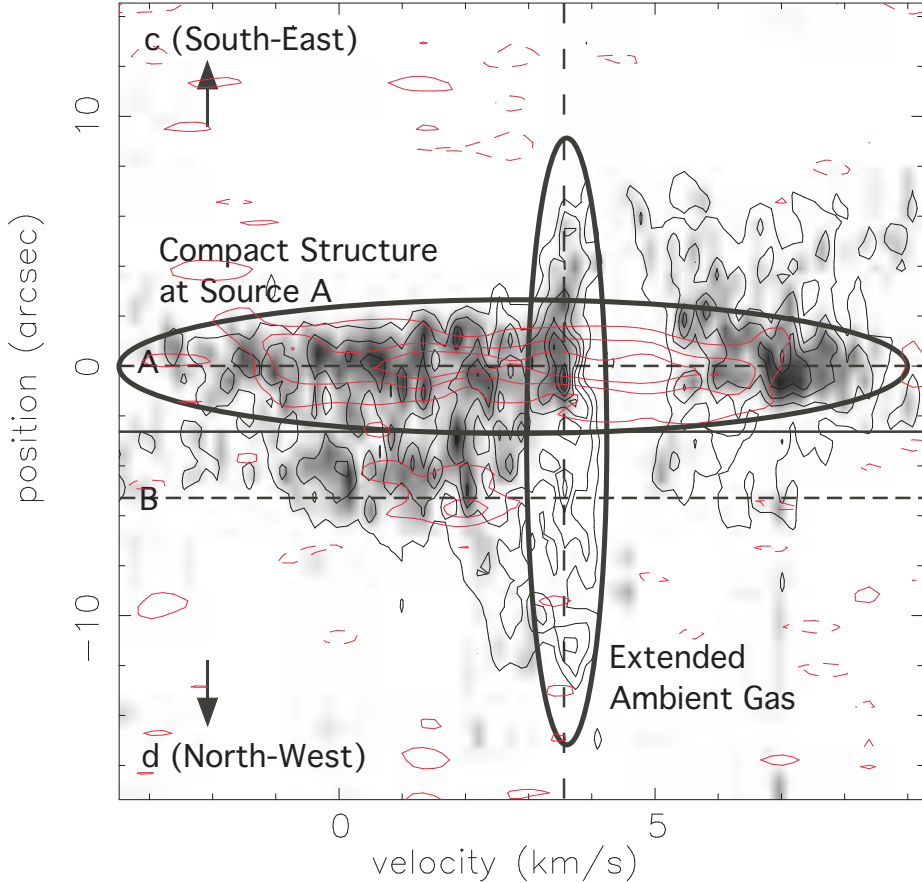


Fig. 8.— P-V diagrams in the HCN (4-3) line with the SMA + JCMT (black contour) and SMA (gray) and in the HC^{15}N (4-3) line with the SMA (red contour), along the axis joining sources A and B (P.A. = 139°). Contour levels are from 11.2 (K) in steps of 11.2 (K) in the HCN emission and from 4.23 (K) in steps of 4.23 (K) in the HC^{15}N emission. Upper and lower horizontal dashed lines show the position of Source A and Source B, respectively, and a vertical dashed line the systemic velocity ($\sim 3.6 \text{ km s}^{-1}$). A solid horizontal line indicates the middle point between Source A and Source B, and should be the binary axis on the assumption of the same mass in Source A and Source B.

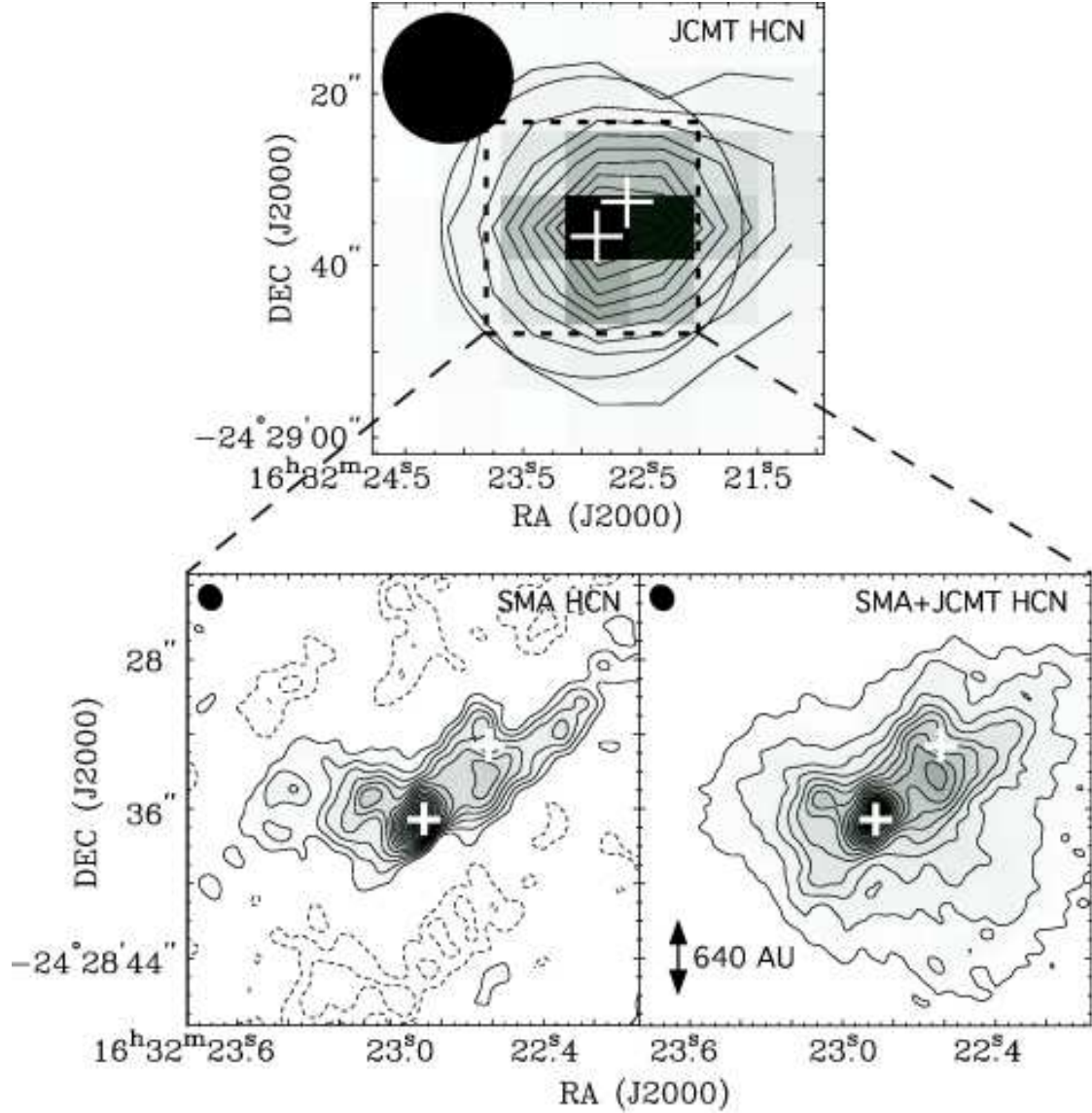


Fig. 9.— Total integrated intensity maps in I16293 taken with JCMT (upper), the SMA (lower-left), and SMA+JCMT (lower-right) in the HCN (4-3) emission. An open circle in the JCMT map indicates the field of view of the SMA, and crosses in each panel indicate positions of the protobinary (Fig.1, Table 2). Filled ellipses at the top left corner of each panel show the synthesized beam, that is, $15''$ in the JCMT map and $1''.3 \times 1''.2$ (P.A. = 30°) in the SMA and the combined map. Contour levels are from 4.76 K km s^{-1} in steps of 4.76 K km s^{-1} in the JCMT map, and from $33.50 \text{ K km s}^{-1}$ in steps of $22.33 \text{ K km s}^{-1}$ in the SMA and combined map.

Table 1. Parameters for the SMA Observations of IRAS 16293-2422

Parameter	Value		
	2003 March 14	2003 July 12	2004 June 19
Number of Antennas	5	4	5
Right Ascension (J2000)		16 ^h 32 ^m 22 ^s .91	
Declination (J2000)		-24°28' 35.52"	
Primary Beam HPBW		~ 35"	
Synthesized Beam HPBW (HCN)	1''.3 × 1''.2 (P.A. = 30°)		
Synthesized Beam HPBW (HC ¹⁵ N)	1''.6 × 1''.3 (P.A. = 14°)		
Synthesized Beam HPBW (Continuum; uniform)	1''.1 × 0''.6 (P.A. = 39°)		
Baseline Coverage		10 - 223 (kλ)	
Conversion Factor (Line)	1 (Jy beam ⁻¹) = 6.2 (K)		
Frequency Resolution (HCN)	203.125 kHz	~ 0.172 km s ⁻¹	
Frequency Resolution (HC ¹⁵ N)	812.5 kHz	~ 0.708 km s ⁻¹	
Bandwidth	82 MHz × 8	82 MHz × 12	82 MHz × 24
Gain Calibrator	nrao530	1743-038	1743-038
Flux of the Gain Calibrator	1.5 Jy	1.5 Jy	2.3 Jy
Passband Calibrator	Mars	Mars, Uranus	Jupiter, Uranus 3c279, 1924-292
Flux Calibrator	Callisto	Uranus	Uranus
System Temperature (DSB)		~ 350 K	
rms noise level (Continuum)		~ 0.06 Jy beam ⁻¹	
rms noise level (Line; SMA + JCMT)		~ 0.9 Jy beam ⁻¹ / 203.125 kHz	

Table 2. 354.5 GHz Continuum Results in I16293 with the SMA

Protostar	R.A. ^a (J2000)	Decl. ^a (J2000)	Deconvolved FWHM Size ^a (AU × AU)	P.A. ^a (°)	Total Flux ^a (mJy)
Source A	16 ^h 32 ^m 22 ^s .87	-24°28'36"6	300 × 150	32.6	3840
Source B	16 ^h 32 ^m 22 ^s .62	-24°28'32"6	150 × 140	24.8	4050

^aEstimated from 2-dimensional Gaussian fittings to the image.